

Origin of the second peak in the mechanical loss function of amorphous silica

Chris R. Billman, Jonathan P. Trinastic, Dustin J. Davis, Rashid Hamdan, and Hai-Ping Cheng

Department of Physics and Quantum Theory Project, University of Florida, 2001 Museum Road, Gainesville, Florida 32611, USA

(Received 4 August 2016; revised manuscript received 7 November 2016; published 23 January 2017)

The thermal noise in amorphous oxides is the limiting factor for gravitational wave detectors and other high-precision optical devices. Through the fluctuation-dissipation theorem, the thermal noise is directly connected to the internal friction (Q^{-1}). Computational calculations of Q^{-1} that use a two-level system (TLS) model have previously been performed for several coating materials, facilitating the search for coatings with lower thermal noise. However, they are based on a historical approximation made within the TLS model that treats the TLS distribution as uncorrelated, which has limited the predictive power of the model. In this paper, we demonstrate that this approximation limits the physical description of amorphous oxides using the TLS model and a fully correlated distribution must be used to calculate high-temperature behavior. Not only does using a correlated distribution improve the theoretical standing of the TLS model, calculations of Q^{-1} using a fully correlated distribution reproduce and uncover the physical mechanisms of a second peak observed in measurements of ion-beam sputtered amorphous silica. We also explore the details of the thermal activation of TLSs and analyze the atomic transitions that contribute to Q^{-1} in amorphous silica.

DOI: [10.1103/PhysRevB.95.014109](https://doi.org/10.1103/PhysRevB.95.014109)**I. INTRODUCTION**

The laser interferometer gravitational-wave observatory (LIGO) recently announced the first detection of gravitational waves, which could usher in a new age of gravitational-wave astronomy [1]. The discovery was made using measurements of the path length of light with accuracy to 10^{-18} m, demonstrating incredible control over the noise sources present in the detector. In the range of ~ 30 – 500 Hz, the limiting noise source for Advanced LIGO is thermal noise in the reflective coatings on the masses at each end of the interferometer [2]. These reflective coatings, consisting of alternating layers of amorphous silica and titania-doped tantala layers, allow the interferometer to detect small changes in the path length due to gravitational waves [3,4]. The thermal noise in the coatings is directly related to the internal friction (Q^{-1}) through the fluctuation-dissipation theorem, providing a clear way to measure the performance of coatings in experiment and simulation [5]. Lowering the internal friction in the coatings is necessary to increase the sensitivity of future gravitational-wave detectors, but there is no clear theoretical path to guide material design for this goal.

The internal friction of amorphous oxides is understood using a two-level system (TLS) model, which was developed to explain anomalous measurements of heat capacity, thermal conductivity, and internal friction at temperatures below 1 K [6–8]. The internal friction in amorphous oxides is modeled by an ensemble of TLSs in which each TLS contributes to the internal friction of the material by coupling to a mechanical field, which causes excitations in the TLS and subsequent relaxation [9]. By finding the TLS distribution, the coupling to a mechanical field, and the relaxation time, one can reproduce the low-temperature behavior seen in experiments. Although the model was developed to explore tunneling, which is only valid at low temperatures, it can be expanded to explain higher-temperature phenomena by including thermal hopping between the two-level systems [9,10]. TLS properties of amorphous oxides continue to be a source of interest, and recent experimental measurements

suggest that controlling the deposition process can have a profound effect on Q^{-1} by lowering the density of TLSs in the system [11–13]. These experimental findings suggest that properties of amorphous materials are very sensitive to the constraints of the system. A connection between the constraints, deposition process, and Q^{-1} is an important path toward the functional design of amorphous materials with lower mechanical loss. The complexity of these systems make computational studies of amorphous materials a powerful tool toward a deeper understanding of the mechanical loss and thermal noise.

Because of the abundance of information on silica [14–21] and its presence in the LIGO mirror coatings, it is a good prototype material to explore the predictive power of a computational application of the two-level system model. Recently, a computational scheme has been developed within classical molecular dynamics (MD) to calculate Q^{-1} of amorphous oxides [22]. The computational scheme explores the potential energy landscape and calculates properties of atomic transitions to generate a distribution of TLSs and other input parameters for the TLS model presented by Gilroy and Phillips [10]. This method has been applied to silica and tantala, and shows the low-temperature peak characteristic of Q^{-1} measurements in amorphous oxides [22,23]. Both silica and tantala calculations match the low-temperature peak within 10 K and the magnitude of the peak within an order of magnitude. While simulated data of bulk silica [14] show a much slower decay after the peak than experimental measurements, it matches the low-temperature peak in ion-beam sputtered (IBS) thin-film measurements [21] very closely.

However, most treatments of the thermally activated TLS model contain an unphysical assumption in the treatment of the TLS distribution that has prevented improvement in computational applications. The loss caused by a TLS depends on the reaction barrier (V) and the asymmetry between minima (Δ). Then, calculations of Q^{-1} require a TLS distribution that depends on these parameters. Throughout the history of the TLS model, the dependence on V and Δ is assumed to be uncorrelated [6,9,10,24–27]. Even though many authors have

debated about the form of the TLS distribution [28–32], the vast majority treat the distributions over V and Δ separately. As we show in this paper, this assumption is contradictory to the definition of a TLS and does not match the distribution obtained in computational simulations. In order to recover the characteristic low-temperature peak using a separated distribution, previous authors introduced an *ad hoc* cutoff in the distribution, in which TLSs with Δ above a fitted cutoff (Δ_{cut}) are eliminated from the distribution [22,23]. The cutoff is a fitting parameter, chosen solely to force agreement with the experimentally measured low-temperature behavior. This cutoff has no theoretical justification and eliminates a majority of the two-level systems discovered in the material, preventing improvement of the model and a detailed physical analysis of the TLSs that lead to mechanical loss. While introducing Δ_{cut} does improve the location of the low-temperature peak, the computational model fails to reproduce high-temperature behavior in either bulk or IBS silica. The inability of previous calculations to agree with experimental measurements beyond the low-temperature peak prevents the method from being used as a predictive tool for advanced LIGO, which will run at temperatures extending beyond the position of the low-temperature peak.

In this paper, we show that using the fully correlated distribution recovers the low-temperature behavior seen in bulk and thin-film experiments without introducing the *ad hoc* cutoff. This conclusively demonstrates that the distribution is intrinsically correlated and must be treated as such to match the character of Q^{-1} in amorphous oxides. Not only does using the fully correlated distribution improve the theoretical standing of the TLS model, it also provides a calculated Q^{-1} that agrees with IBS silica up to ~ 150 K. Using the fully correlated distribution allows a direct connection between details in the calculated Q^{-1} and individual TLSs, which we explore in this paper. This development demonstrates the applicability of the model near room temperature and opens avenues for future developments that better describe the coupling of individual TLSs to fluctuations in amorphous oxides.

The paper is organized as follows. Section II introduces the TLS model, previous approximations made, and how this method improves upon them. In Sec. II A, we introduce the TLS model. Section II B describes the different distributions that can be used in the TLS model and Sec. II C details the MD methods and generation of parameters for the TLS model. In Sec. III, we present the results, showing improvement in the description of the internal friction in silica using a correlated distribution. In Sec. III A, we show Q^{-1} calculated with the TLS model. In Sec. III B, we discuss the physics of the different distributions. In Sec. III C, we analyze which two-level systems are thermally activated at specific temperatures. In Sec. III D, we describe the atomic transitions that lead to features in Q^{-1} .

II. METHODS

A. TLS model

Glasses contain many degrees of freedom in their local structure, which leads to a complicated potential energy landscape. It is believed that the underconstrained nature of amorphous materials forms two-level systems (TLSs) throughout the material [11]. Transitions between TLSs are the

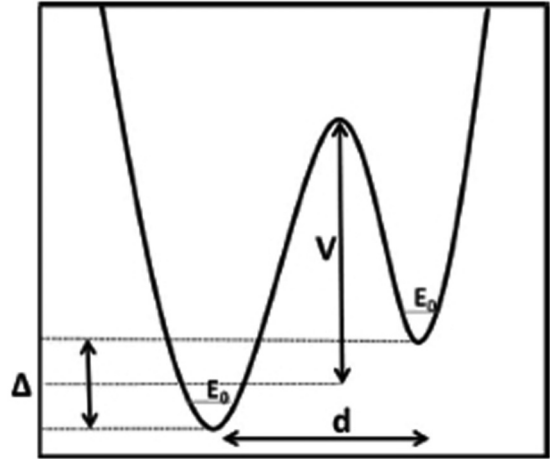


FIG. 1. An illustration of a two-level system (TLS), where Δ is the asymmetry, V is the average barrier height, E_0 is the ground-state energy of the state in each well, and d is the configurational distance between the wells.

primary source of mechanical loss, thermal conductivity, and heat capacity in amorphous oxides at low temperature [10,11]. TLSs can be described by two parameters: the asymmetry (Δ) and the barrier height (V), shown schematically in Fig. 1. Because of a coupling (γ) of each two-level system to a mechanical field, acoustic waves induce transitions which lead to mechanical loss. As a material has many TLSs, the contribution from each must be summed, which gives the following expression for the internal friction [9,10]:

$$Q^{-1} = \frac{\gamma^2}{3\epsilon k_b T} \iint \frac{\omega \tau}{1 + \omega^2 \tau^2} \frac{\Delta^2}{E^2} \text{sech}^2\left(\frac{E}{2k_b T}\right) \times g(\tau, E) d\tau dE, \quad (1)$$

where ϵ is the the appropriate elastic modulus, ω is the angular frequency of the acoustic wave, τ is the relaxation time of the TLS, E is the energy splitting between the two states of the TLS, and $g(\tau, E)$ is the number density of TLSs. As this paper focuses on the internal friction caused by longitudinal waves, the Young's modulus and the longitudinal coupling constant were calculated and used for ϵ and γ in this expression.

The energy splitting for TLSs is given by

$$E^2 = \sqrt{\Delta^2 + \Delta_0^2}, \quad (2)$$

where Δ_0 is the tunneling splitting. The tunneling splitting is given by

$$\Delta_0 = 2\langle \phi_1 | H | \phi_2 \rangle, \quad (3)$$

where ϕ_1 is the state in the first well, ϕ_2 is the state in the second well, and H is the Hamiltonian of the system. Because the effective particle in the TLS is not well understood, it is not clear how to evaluate Δ_0 directly. Previous work estimates that the tunneling splitting is of the order of 10^{-4} eV [8,9]. For this reason, this work uses a constant $\Delta_0 = 10^{-4}$ eV, and replaces $g(\tau, E)$ with $g(\tau, \Delta)$. Several different values of Δ_0 were tested, and the calculated Q^{-1} does not change significantly as long as Δ_0 is within one order of magnitude of 10^{-4} eV.

The relaxation time of thermal hopping in the two-level system can be found using an Arrhenius rate law,

$$\tau^{-1} = \tau_0^{-1} \cosh\left(\frac{\Delta}{2k_b T}\right) e^{-\frac{V}{k_b T}}. \quad (4)$$

The attempt frequency τ_0^{-1} is calculated from the vibrational modes of the system with the equation

$$\tau_0^{-1} = \frac{\prod_{i=1}^{3N} v_i^0}{\prod_{i=1}^{3N-1} v_i^s} e^{\frac{S}{k_b}}, \quad (5)$$

where v^0 are the vibrational frequencies at the minimum, v^s are the vibrational frequencies at the saddle point, and S is the contribution to the free energy from the entropy of the transition states [33]. Although $\frac{S}{k_b} = \ln(2)$ would be expected for a TLS model, previous studies of TLSs in silica use $\frac{S}{k_b} = \ln(4)$, as it better fits experimental data [14,22]. The exponential dependence of the relaxation time on V and Δ means that variations in V and Δ will change the relaxation time by larger amounts than τ_0 . As the calculation of τ_0 requires expensive calculations of the Hessian matrix, and the effect of V and Δ is more substantial, we compute the average τ_0 for the system. Because the relaxation time is a function of only the asymmetry and barrier height of the TLSs, $g(\tau, \Delta)$ is replaced by $N(V, \Delta)$:

$$Q^{-1} = \frac{\gamma^2}{3\epsilon k_b T} \iint \frac{\omega \tau}{1 + \omega^2 \tau^2} \frac{\Delta^2}{E^2} \times \text{sech}^2\left(\frac{E}{2k_b T}\right) N(V, \Delta) dV d\Delta. \quad (6)$$

B. Distribution of two-level systems

Simulated Q^{-1} depends very heavily on the details of the TLS distribution. In the derivations above, the distribution is fully correlated,

$$N_{\text{corr}}(V, \Delta) = N(V, \Delta). \quad (7)$$

However, all previous works [10,22–24,26,27] separate the two-dimensional (2D) distribution over the barrier height and asymmetry into the product of 1D distributions:

$$N_{\text{sep}}(V, \Delta) = g(V)f(\Delta). \quad (8)$$

Not only does this ease analytic calculations of Q^{-1} , it also decreases the amount of discovered TLSs needed to converge the total distribution. This is related to the ‘‘curse of dimensionality’’: data points separated into N bins in uncorrelated histograms for V and Δ are separated into N^2 bins for the correlated histogram. This means that converging $N_{\text{corr}}(V, \Delta)$ requires much more computational time. The accuracy of this approximation relies on the absence of correlation between the barrier height and asymmetry. This cannot be true, as at the very least they must be related by

$$\Delta < 2V. \quad (9)$$

A TLS system is not defined for $\Delta \leq 2V$ because this corresponds to a system with no barrier (Fig. 1). Then, any accurate TLS distribution should show no states for $\Delta \leq 2V$.

The comparison of the two treatments of the TLS distribution is shown in Fig. 2. In Fig. 2(a), $N_{\text{corr}}(V, \Delta)$ shows a sharp

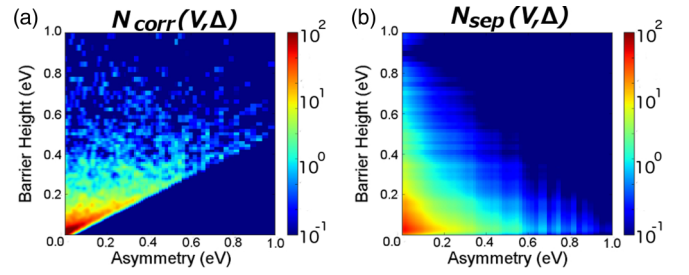


FIG. 2. Logarithmic heat maps of the TLS distribution calculated in amorphous silica using the (a) fully correlated 2D distribution $N_{\text{corr}}(V, \Delta)$ and (b) separable 1D distributions $N_{\text{sep}}(V, \Delta)$.

division between regions with states and a dark blue region with no states. The line that separates these regions is $\Delta = 2V$, shifted down slightly due to the smearing effect of constructing a distribution using a kernel density estimate (described in more detail in the next section). This line is the constraint in Eq. (9), demonstrating that $N_{\text{corr}}(V, \Delta)$ only has states with a barrier between the minima (Fig. 1). However, $N_{\text{sep}}(V, \Delta)$ [Fig. 2(b)] does not show this sharp line and contains many states below it. Separating the dependence on V and Δ leads to a distribution that has states in a region where a TLS is not properly defined. Beyond the violation of the definition of a TLS, $N_{\text{sep}}(V, \Delta)$ describes a very different distribution than $N_{\text{corr}}(V, \Delta)$. $N_{\text{sep}}(V, \Delta)$ has a distribution that is very wide at low barrier height and narrows as it moves to higher barrier height, while $N_{\text{corr}}(V, \Delta)$ is very narrow at low barrier height and widens as it moves to higher barrier height. The only region where they agree is at low barrier height and asymmetry, where both distributions show the highest density.

To improve comparison with experiment, the work that calculates Q^{-1} with a separated distribution also introduces a 0.1 eV asymmetry cutoff [22,23] to better match experiment. This distribution is defined as

$$N_{\text{cut}}(V, \Delta) = g(V)f(\Delta)\Theta(\Delta_{\text{cut}} - \Delta), \quad (10)$$

where Θ is the Heaviside step function and, in this case, $\Delta_{\text{cut}} = 0.1$ eV. The choice is motivated by a study finding defects that emerge at higher temperature which are not seen in experiment [25,34], and by the sech^2 term, which should prevent TLSs above the cutoff to contribute significantly. Like N_{sep} , this offers easier analytic computability and a more rapid convergence of the distribution.

C. MD simulation details

All parameters [Δ , V , $N(V, \Delta)$, τ_0 , γ , and ϵ] for the internal friction are obtained through classical molecular dynamics (MD) simulations. Then, the loss is calculated according to Eq. (6). The MD simulations are performed using the DLPOLY package [35], with the ridge method and other extensions developed within our group as described in more detail in a previous publication [22]. The simulation is composed of 720 atoms, i.e., 240 Si atoms and 480 O atoms with periodic boundary conditions, so that the simulation should resemble bulk silica. The force fields are based on the Beest, Kramer, and van Santen (BKS) potential [36,37].

Atomic configurations are obtained by annealing a crystalline cristobalite sample to 8000 K, which provides an amorphous sample. The annealing is done in an NPT ensemble, starting at 300 K and increasing in intervals of 200 K. Each interval is performed for 6 ps, except for the peak temperature which is run for 20 ps. After quenching the temperature back to 300 K, the configuration is equilibrated for 30 ps in an NPT ensemble, and then 30 ps in an NVT ensemble.

The TLS search consists of two steps: the bisection method and the ridge method. A trajectory is obtained using an MD simulation of the amorphous oxide, run in an NVT ensemble using a Nosé thermostat. From that trajectory, the bisection method obtains two adjacent time steps that relax to separate minima. These minima configurations are used as input for the ridge method, which searches for a saddle point between the minima. If the ridge method finds a single saddle point between the minima found during the bisection method, the minima are connected and a TLS is found. Each TLS is described by the asymmetry (Δ) and the average barrier height (V):

$$\Delta = E_2 - E_1, \quad (11)$$

$$V = \frac{1}{2}[(E_s - E_1) + (E_s - E_2)], \quad (12)$$

where E_s is the energy at the saddle point, E_1 is the energy at the first minimum, and E_2 is the energy at the second minimum. The distribution functions $N(V, \Delta)$, $g(V)$, and $f(\Delta)$ (described in Sec. II B) are calculated by constructing a kernel density estimation from the discovered TLSs. This generates a smooth, continuous distribution function by placing a Gaussian function at every data point corresponding to a discovered TLS. A subset of these atomic configurations is later used to calculate the average coupling constant γ and average attempt frequency τ_0^{-1} .

To better sample the potential landscape, 15 configurations are generated using the annealing process described above. The pair-distribution function of all configurations shows good agreement with experiment, demonstrating that configurations recover the short-range order of experimentally generated bulk silica. After annealing, barrier searches are conducted for each configuration. These different configurations are generated using an NPT ensemble, but all have lattice parameters very close to 21 Å.

Some annealed configurations yield barrier searches that are trapped in a part of the potential landscape that does not show the same physics as experiment, in which the peak in Q^{-1} (T_{peak}) occurs at higher temperature. These configurations were not found in previous searches [22,23], as fewer configurations were necessary to converge the separated distributions used in those works. It may be possible that these anomalous configurations are also present but suppressed in experimental materials and that our method of generating configurations shows preference for them. As computational limitations prevent simulations that match the time scales of experimental annealing, there is no clear way to limit computational modeling to the region of the potential energy landscape (PEL) sampled by experiment [38]. Therefore, there is no way to ensure that the generated configuration matches experimental samples except by comparing the physical properties of the resulting configurations. Including all configurations in the

calculation yields T_{peak} and peak Q^{-1} close to experiment, but the loss function lacks the broad low-temperature peak which is characteristic of the loss in amorphous materials or the second peak seen in IBS silica.

In order to qualitatively explore the second peak, the majority subset of configurations that reproduce a low-temperature peak ($T_{\text{peak}} < 50$ K) is used to construct the distribution of TLSs. This selection process is an attempt to bring the results of MD simulation closer to experimental conditions, similar to that used to study crystals where simulations begin from structures that match experimental measurements (lattice parameters, bond lengths, etc.), but may introduce a bias into our results. If the selection process is masking the inability of the melt-quench method to reach the region of the PEL truly responsible for the second peak, then descriptions of the second peak in this manuscript will not be true.

This methodology allows calculations of Q^{-1} to combine diverse regions of the potential landscape in the same way that an experiment will measure the loss over the varying configurations that make up the bulk material.

III. RESULTS

A. Internal friction

Figure 3 contains plots of the calculations of Q^{-1} using the correlated distribution [$N_{\text{corr}}(V, \Delta)$], the separated distribution [$N_{\text{sep}}(V, \Delta)$], and the cutoff distribution [$N_{\text{cut}}(V, \Delta)$] compared to experimental measurements of Q^{-1} in bulk amorphous silica [14] and ion-beam sputtered (IBS) silica [21]. The calculations and IBS measurements were done at 1118 Hz, and the bulk measurement at 11 400 Hz. Calculations of Q^{-1} with the fully correlated distribution (red curve) show a broad low-temperature peak with a sharp spike at 12 K and several shoulders. This compares very well with the IBS data (black solid curve), which has a peak at 18 K and a peak magnitude that differs by only 50% of peak, Q_{IBS}^{-1} . After 60 K, Q_{corr}^{-1} plateaus until a second peak at 114 K. This also compares well to Q_{IBS}^{-1} , which has additional peaks at ~ 150 and ~ 250 K. Although Q_{corr}^{-1} does not show a third peak, the

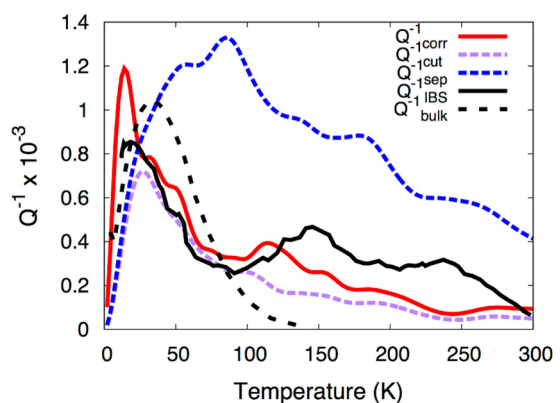


FIG. 3. Calculated mechanical loss as a function of temperature using a correlated TLS distribution (Q_{corr}^{-1}), separated TLS distribution with cutoff (Q_{cut}^{-1}), and separated TLS distribution without cutoff (Q_{sep}^{-1}). These are compared to experimental measurements of mechanical loss of IBS silica (Q_{IBS}^{-1}) [21] and bulk silica (Q_{bulk}^{-1}) [14].

value at room temperature differs by less than 5% of Q_{IBS}^{-1} . The peak magnitude of Q_{corr}^{-1} is closer to that of Q_{bulk}^{-1} (black dashed curve) but does not match the temperature dependence, in which T_{peak} is ~ 30 K and there is a rapid, monotonic decay beyond 50 K.

The calculated Q^{-1} using the two different approximations (discussed in Sec. II B) can be evaluated and compared to the full level of theory captured by $N_{\text{corr}}(V, \Delta)$. It is clear from Q_{sep}^{-1} (blue dashed curve) that a separable distribution does not correctly describe the physics in amorphous silica. The curve peaks at 86 K and is two to four factors larger than Q_{corr}^{-1} above 40 K. These calculations do not even reproduce the characteristic shape of $Q^{-1}(T)$, which is a low-temperature peak followed by a rapid decay.

Calculated Q^{-1} using $N_{\text{cut}}(V, \Delta)$ (purple dashed curve) compares much better, with a peak at 28 K followed by a rapid dropoff until ~ 60 K and then a slower decrease until 300 K. However, it is missing the sharp peak at 12 K and the second peak at 120 K. It also underestimates the magnitude of Q^{-1} throughout the temperature range plotted in Fig. 3. While Q_{cut}^{-1} does have a similar shape as Q_{corr}^{-1} , it does not capture the finer features obtained using the $N_{\text{corr}}(V, \Delta)$.

B. Distribution analysis

From Figs. 2 and 3, it is evident that using a separable distribution is not theoretically justified and gives poor results for Q^{-1} in silica. It is curious that introducing a cutoff improves calculations of Q^{-1} and compares well to experimentally measured values. To understand the effect of introducing a cutoff in the separable distribution, the three TLS distributions need to be examined in detail. In Fig. 4, $N_{\text{corr}}(V, \Delta)$, $N_{\text{sep}}(V, \Delta)$, and $N_{\text{cut}}(V, \Delta)$ are plotted for the region below the 0.1 eV cutoff in Δ in $N_{\text{cut}}(V, \Delta)$. Because of the presence of the sech^2 term in Eq. (6), this is the area of the TLS distribution that contributes most significantly to Q^{-1} . All three figures show the highest density at low barrier height and asymmetry. However, the

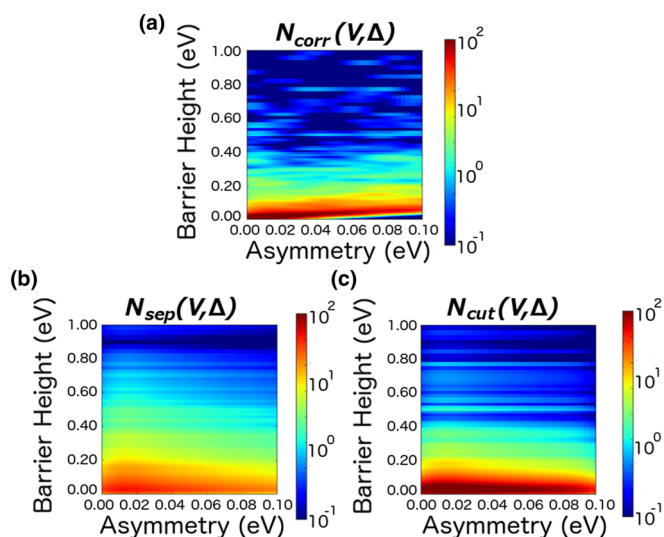


FIG. 4. Logarithmic heat maps of (a) $N_{\text{corr}}(V, \Delta)$, (b) $N_{\text{sep}}(V, \Delta)$, and (c) $N_{\text{cut}}(V, \Delta)$ plotted for $\Delta < 0.1$ eV.

details of each distribution beyond this similarity do not agree across the three methods.

Both $N_{\text{sep}}(V, \Delta)$ and $N_{\text{cut}}(V, \Delta)$ lack the condition shown in Eq. (9). This condition is seen most clearly in Fig. 2(a) as the diagonal line which divides the distribution between a region with finite density and the blue region with zero density. This diagonal line is present, though barely visible, in Fig. 4(a), but is not present in Figs. 4(b) and 4(c). Because this condition introduces a correlation, it is necessary to examine the consequences of separating a correlated distribution. In a separated distribution, a TLS discovered at particular (V, Δ) is replicated at every other (V', Δ) in the 2D distribution. In the TLS distribution, this means that a discovered TLS that follows the physical condition that $\Delta < 2V$ will be replicated in regions that violate this condition. We refer to TLSs that are introduced in this way as “replica TLSs.”

The differences between $N_{\text{corr}}(V, \Delta)$ and $N_{\text{sep}}(V, \Delta)$ can primarily be explained by using this concept of replica TLSs. At large barrier height, the constraint in Eq. (9) corresponds to a wide area of Δ which has high probability. For instance, $N_{\text{corr}}(V, \Delta)$ [Fig. 4(a)] has high density for $V = 0.10$ eV across the entire 0.1 eV Δ range plotted, some of which are in the red band of high density along the diagonal line. TLSs with large Δ will be replicated with small barrier height, leading to the red horizontal band at $V = 0$ in Figs. 4(b) and 4(c). At large barrier height, the density of TLSs in $N_{\text{corr}}(V, \Delta)$ is highest at large Δ , but because $N_{\text{sep}}(V, \Delta)$ neglects the correlation, it is incorrectly peaked at low Δ for all V .

This directly leads to the errors present in Q_{sep}^{-1} . At low V , which corresponds to the TLSs activated at low temperature, replica TLSs shift the density to higher Δ compared to $N_{\text{corr}}(V, \Delta)$. Because of the sech^2 term, TLSs with larger Δ cannot be thermally excited and do not contribute to Q^{-1} . This causes Q_{sep}^{-1} to underestimate Q_{corr}^{-1} at low temperature. At high V , which corresponds to the TLSs activated at high temperature, replica TLSs shift the density to lower Δ compared to $N_{\text{corr}}(V, \Delta)$. This causes more TLSs to be thermally activated and contribute to Q^{-1} , causing the large values of Q_{sep}^{-1} above 50 K.

Introducing a cutoff mitigates the errors created by separating the TLS distribution because it eliminates the most problematic replica TLSs. By eliminating TLSs with large Δ , the 1D distribution $f(\Delta)$ does not significantly suppress the TLS distribution at low Δ and low V , which improves low-temperature Q^{-1} . It corrects for high-temperature Q^{-1} because it forces the density to be lower at higher V by removing the majority of TLSs with large V . The effect of removing all of these TLSs is demonstrated by the dark blue horizontal bands in Fig. 4(c), where $g(V)$ is zero because the TLSs discovered at that barrier height are above the cutoff in Δ .

The process of fitting the cutoff (Δ_{cut}) is effectively fitting a window of agreement with $N_{\text{corr}}(V, \Delta)$ in the thermally activated region. Regions in the middle of the window are not affected by the violation of Eq. (9), which is the primary error that results from separating the distribution. The efficacy at the top of the window is limited because TLSs at and above Δ_{cut} will become thermally excited and will contribute to Q^{-1} . The window is limited at the bottom because there will still be a point at which replica TLSs will shift the density to higher

Δ . For the choice of $\Delta_{\text{cut}} = 0.1$ eV, replica TLSs will violate the constraint $\Delta < 2V$ for V less than 0.05 eV. As we will show in Sec. III C, this corresponds to the sharp 12 K peak in Q_{corr}^{-1} . Fitting Δ_{cut} can shift the window where Q_{corr}^{-1} and Q_{sep}^{-1} agree on broad features, but it is impossible to prevent replica TLSs from introducing errors outside the window.

At this point, it is not possible to see the reason that the Q_{cut}^{-1} does not have a peak at 130 K. However, it is already evident that the violation of the physical definition of a TLS and the lack of correlation present in $N_{\text{cut}}(V, \Delta)$ prevent it from going beyond matching the shape of Q^{-1} . Matching details at and above 300 K, where the sech^2 will no longer effectively eliminate TLSs above 0.1 eV, requires the use of $N_{\text{corr}}(V, \Delta)$.

C. TLS activation

Identifying the activated two-level systems at a given temperature is an important link between features in the Q^{-1} plots and the atomic transitions that cause them. Moreover, this identification can clarify the finer differences between the $N_{\text{corr}}(V, \Delta)$ and $N_{\text{cut}}(V, \Delta)$. To visualize the activated TLSs, we plot the function

$$q^{-1}(V, \Delta; T) = \left(\frac{\omega\tau}{1 + \omega^2\tau^2} \right) \left[\frac{1}{k_b T} \frac{\Delta^2}{E^2} \text{sech}^2 \left(\frac{E}{2k_b T} \right) \right] \times N(V, \Delta), \quad (13)$$

which is just the integrand in Eq. (6). This function combines the TLS distribution with the details of the excitation. The first factor captures the resonance between the ensemble of TLSs with acoustic wave with frequency ω . The second factor is the average polarizability of an ensemble of TLSs with asymmetry Δ and contains the information about the interaction between the TLS and the stress field. The product of these two terms and the TLS distribution describes which TLSs contribute to the mechanical loss at a particular temperature. The plots of $q^{-1}(V, \Delta; T)$ for $N_{\text{corr}}(V, \Delta)$ and $N_{\text{cut}}(V, \Delta)$ are shown in Fig. 5.

As the temperature increases, a larger area of TLSs is activated thermally. This is because the relaxation time for TLSs contains exponential dependence on both V and Δ divided by the temperature, shown by Eq. (4). When the temperature increases, the relaxation time varies more slowly with V and Δ . This leads to the activation of a larger area of the TLS distribution. Despite the small area of activation at low temperature, the very high density of TLSs with small barrier height and asymmetry results in a large peaked value of mechanical loss at low temperature. Using the insets in Figs. 5(a) and 5(b), one can see that the area activated for $N_{\text{corr}}(V, \Delta)$ is slightly larger than for $N_{\text{cut}}(V, \Delta)$. This is because the density is higher for $N_{\text{corr}}(V, \Delta)$ for small V , which causes the larger value of Q^{-1} at 12 K and leads to a sharp spike that sits atop the broad low-temperature peak between 0 and ~ 60 K. The density of TLSs with small V is underestimated by the separable distribution in this region because of the effect of ‘‘replica TLSs’’ (discussed in Sec. III B), causing $Q_{\text{cut}}^{-1}(T)$ to peak at higher temperature.

The second peak (Fig. 3) in the mechanical loss found in calculations using $N_{\text{corr}}(V, \Delta)$ occurs at ~ 120 K. At this temperature, barriers between 0.15 and 0.25 eV are the

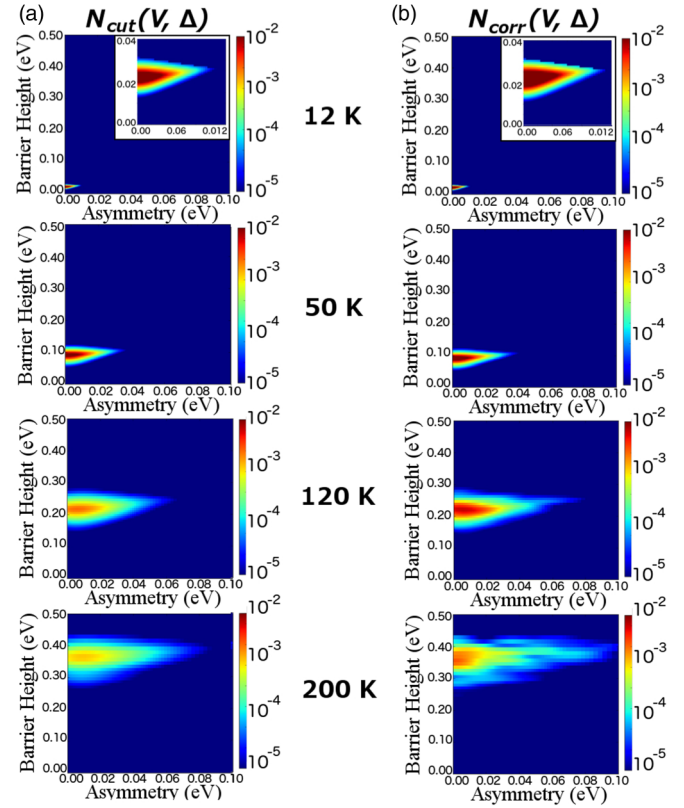


FIG. 5. (a) Plots of $q^{-1}(V, \Delta; T)$, defined in Eq. (13), for different temperatures for the separable 1D distribution. (b) Plots of $q^{-1}(V, \Delta; T)$, defined in Eq. (13), for different temperatures for the 2D distribution. The insets for 12 K plots show a smaller range, in order to show the contributing TLSs.

primary contributors. However, the separable distribution does not capture the increased density at lower asymmetry here. Because it shifts the density to higher asymmetry, the separable distribution prevents TLSs in this range from being thermally activated and contributing to the mechanical loss. Because the increased density of TLSs in the 0.15 to 0.25 eV range only happens for small asymmetry, which is a clear sign of correlation, a separated distribution is not able to reproduce the feature and will miss features such as the second peak in Q^{-1} . At 200 K, there is still a slight underestimation of TLSs at low asymmetry by the separable distribution, which causes a small disagreement between the two models. The plot for the 2D distribution at 200 K has irregularities, not seen in plots at any other temperature. These gaps show regions where no TLSs have been discovered. To accurately capture Q^{-1} above 200 K, a better sampling of large V is needed. The gaps in $q^{-1}(V, \Delta; T)$ are a useful sign to show the temperature region in which we can make detailed conclusions. This suggests that capturing higher-temperature behavior requires significantly more TLSs and the lack of convergence may be the reason that Q^{-1} calculated with the $N_{\text{corr}}(V, \Delta)$ does not reproduce the third peak seen in IBS measurements.

Although $N_{\text{corr}}(V, \Delta)$ at and above 200 K shows a lack of convergence, the $N_{\text{cut}}(V, \Delta)$ still looks smooth. These plots also show that barriers close to the 0.1 eV asymmetry cutoff are beginning to contribute to the internal friction,

which shows the risk of using $N_{\text{cut}}(V, \Delta)$. This highlights the complication of fitting a cutoff. The choice of Δ_{cut} that gives good agreement with the low-temperature peak does not describe room-temperature behavior well because loss at higher temperature involves TLSs excited beyond the cutoff. In order to accurately calculate Q^{-1} at and exceeding room temperature, $N_{\text{corr}}(V, \Delta)$ must be used. The only other option is to increase the cutoff, which will decrease the accuracy of low-temperature behavior. However, no matter what window is chosen, the separated distribution will always miss highly correlated features such as the second peak.

The function $q^{-1}(V, \Delta; T)$ not only allows comparison between the different distributions used to calculate the internal friction, it connects features in the Q^{-1} plots and the atomic transitions that create the loss. Using this function, one can link the features that describe Q_{corr}^{-1} to the regions of the TLS distribution. We have identified three features that describe the loss function: the sharp peak at 12 K is composed of TLSs with barrier height smaller than 0.04 eV, the broad peak that decays until ~ 60 K is composed of TLSs with barrier height below 0.1 eV, and the second peak is composed of TLSs with barrier height between 0.15 and 0.25 eV.

D. TLS transitions

By collecting structural statistics for the TLS transitions within the activated ranges identified using $q^{-1}(V, \Delta; T)$, characteristic transitions can be defined for each feature in the Q^{-1} curve. If the sharp spike at 12 K is treated as a separate feature to investigate, there are three regions of interest:

- (i) Sharp peak at 12 K: TLSs with barrier heights below 0.04 eV.
- (ii) Broad peak that ends at ~ 60 K: TLSs with barrier heights between 0.04 and 0.10 eV.
- (iii) Second peak at 114 K: TLSs with barrier heights between 0.15 and 0.25 eV.

Histograms of the most significant descriptors of the transitions that contribute to these three features are shown in Fig. 6. These descriptors are chosen because they show the best separation between distributions of the features defined above. They are as follows:

- (a) Atoms involved in transition: the sum of atoms that have an atomic displacement above 0.1 Å.
- (b) Bond changes: the number of oxygen atoms that changes its nearest silicon neighbor.
- (c) Oxygen rotations: the number of oxygen atoms that rotate more than five degrees around the closest silicon atom.
- (d) Largest oxygen rotation: the largest angle that an oxygen rotates around the closest silicon atom.

As shown in Fig. 6, the histograms for each of these TLS ranges have distinct distributions for transition descriptors. As the temperature increases, the number of atoms involved, number of oxygen rotations, and the maximum rotation angle all increase. Other descriptors, such as the average total motion and the volume of involved atoms, also show this behavior. While this follows physical intuition, there are some outliers. Some TLSs with barrier height less than 0.1 eV still involve 100 atoms. However, the general trend is that the more atoms are involved in the transition, the larger the energy it takes to cause the transition. Because of the variation in the

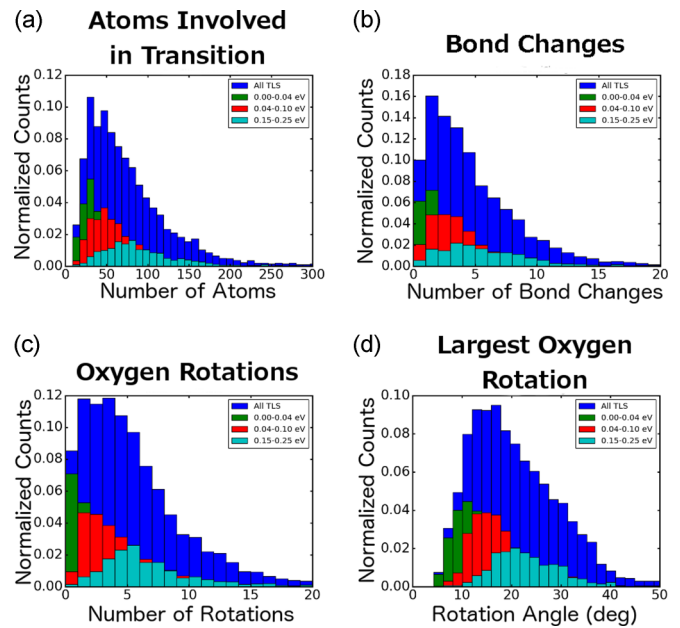


FIG. 6. Histograms show (a) the number of atoms involved in transitions, (b) the number of oxygen atoms that change which Si atom they are bonded to, (c) the number of oxygen atoms that rotate more than five degrees around the cation they are bonded to, and (d) the largest oxygen rotation angle in a TLS transition. The 0.00–0.04 eV distributions correspond to the 12 K peak, 0.04–0.10 eV to the broad low-temperature peak, and 0.15–0.25 eV to the peak at 120 K. These regions are identified by Fig. 5.

descriptors, caused by the amorphous nature of the material, the characteristic transitions can only be described statistically. So, the discussion of transitions that lead to each of the features in Q^{-1} will be described in terms of average values and the spread of those descriptors.

The characteristic transition for TLSs with V less than 0.04 eV consists of ~ 25 atoms, involves less than three atomic rotations or coordination changes, and has a maximum rotation angle of ~ 12 degrees (Fig. 6). The number of rotations is peaked at zero and the number of bond changes is peaked at one. This implies that the 12 K peak is predominantly composed of oxygen atoms rotating and changing the nearest silicon neighbor.

For TLSs with V between 0.04 and 0.1 eV, the characteristic transition involves roughly 50 atoms and has five or fewer oxygen atoms change coordination. The broad peak transitions contain between two and six oxygen atom rotations for this transition and the maximum rotation angle is peaked around 15 degrees. These transitions are still fairly local, but involve the rotations of several polyhedra.

TLSs with V between 0.15 and 0.25 eV have a much wider spread in all of the descriptors. The distribution of transitions involves between 50 and 100 atoms and can have up to ten oxygen atoms change coordination. Transitions that lead to this peak involve around six oxygen rotations, with a maximum rotation between 15 and 30 degrees. This is a single transition composed of the coordinated motion of many polyhedra.

These transitions can be compared to previous proposed loss mechanisms based on experimental studies. Two

mechanisms have been proposed for the low-temperature peak: oxygen hopping between minima in elongated Si-O-Si bonds [39] and torsional rotations of oxygen along Si-O-Si bonds [40]. The transitions with V less than 0.04 eV, described predominantly by a coordination change, match the description of single oxygen hopping along bonds, although the calculated barrier height (~ 0.025 eV) is lower than the 0.05 eV predicted in Lunin's [39] work. The transitions between 0.04 and 0.10 eV seem to be rotations of polyhedra, which could be related to the mechanism suggested by Bartenev [40] but at a larger scale. Our calculations, which show that both of these transitions occur at low temperature, suggest that the low-temperature peak is a result of both Lunin-like and Bartenev-like transitions. Beyond the IBS silica results shown here, other studies have found peaks in the mechanical loss at higher temperature in amorphous silica [27,39,40]. Lunin and Bartenev found excitation peaks well above room temperature and both attribute them to β relaxation, which does not match the predicted energies or the structural description of the second peak seen here. However, the small excitation peaks seen by Travasso occur between 200 and 300 K, and could be caused by a similar mechanism as the second peak in these calculations.

Atomic structures corresponding to characteristic transitions for the broad low-temperature peak and the 120 K peak are shown in Fig. 7. The characteristic transition for the broad, low-temperature peak shows a coordination change in the polyhedron in the middle, and rotations by surrounding polyhedra. The 120 K transition involves twice the atoms and is composed of several polyhedra rotations.

Here, we return to the choice to treat the low-temperature peak as a separate feature. The atoms involved and the largest oxygen rotation show distinct peaks separate from the peaks for the range 0.04 to 0.10 eV. The broad peak should be composed both of TLSs below 0.04 eV as well, but it is not possible to disentangle the different transitions below 0.04 eV. The descriptors show well-defined distributions for both the sharp peak and the broad peak, suggesting that they are, in fact, two separate transitions. Then, it may be that the low-temperature peak observed in Q_{IBS}^{-1} (Fig. 3) is due to two distinct transitions that are activated at the same temperature. Then, the mechanisms proposed by Bartenev and Lunin may both be occurring in the low-temperature peak.

At this point, it is possible to speculate about the differences between calculated Q^{-1} and measurements of both IBS and bulk silica. Bulk measurements of Q^{-1} of silica are characterized by a low-temperature peak that rapidly drops by about an order of magnitude. However, the IBS film and the calculations shown here do not share that behavior. As shown by the plots of $Q^{-1}(V, \Delta; T)$ in Fig. 5, TLSs with V larger than 0.1 eV lead to features above 50 K. Therefore, to agree with bulk measurements, there needs to be a high density of TLSs with V less than 0.1 eV, but a very small density above.

Further insight can be gained by viewing the results of this model in light of other recent work on amorphous oxides. Recent experimental measurements [11] find that deposition techniques can have a powerful role in changing the density of TLSs. By allowing atomic rearrangement during deposition, the authors believe that they reach a higher level of constraint, which quenches the TLS density. A recent computational

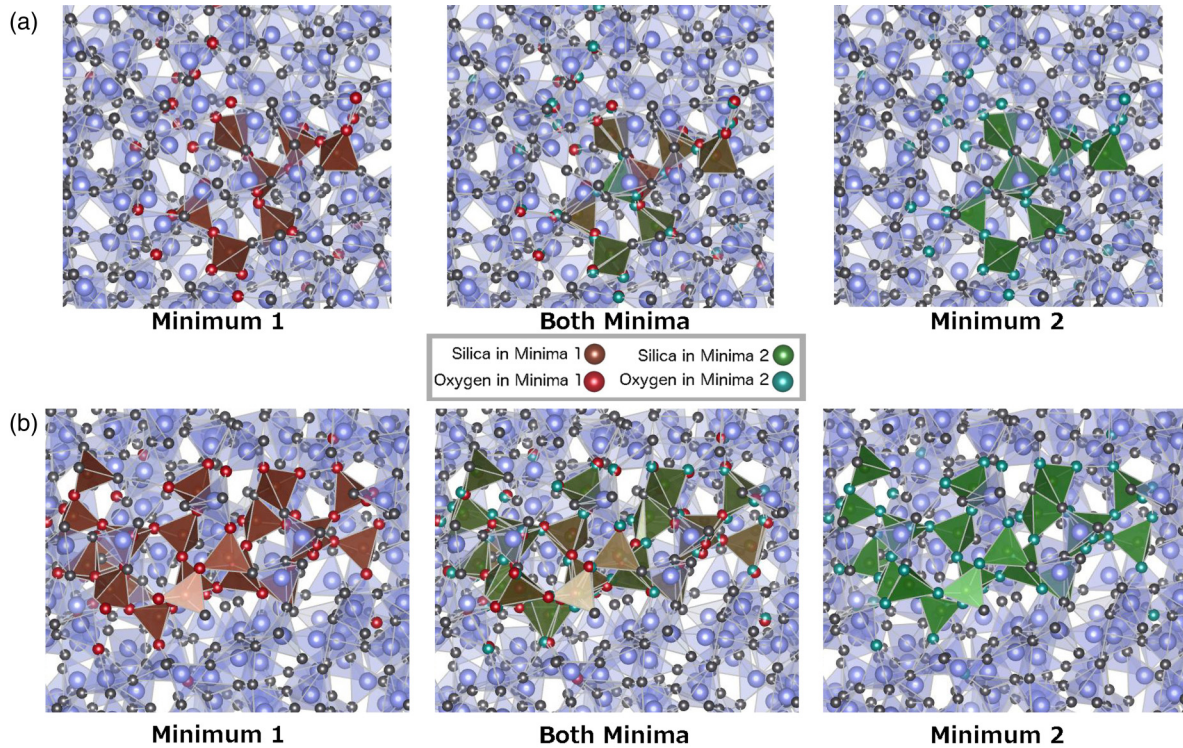


FIG. 7. (a) Atomic structures of the minima of a TLS that is characteristic of the broad low-temperature peak, with 48 atoms involved in the transition. (b) Atomic structures of each minima of a TLS that is characteristic of the peak at 120 K, with 79 atoms involved in the transition. Figures labeled “Both Minima” show the second minimum configuration overlaid on the first so that the transition is clearer.

study of densified sodium silicate, another amorphous oxide, shows that intermediate densities had a “reversibility window,” where the constraints on the system dropped dramatically [41]. These results demonstrate an extreme sensitivity on the environment and constraints in the amorphous oxide. While the MD simulations used to calculate Q^{-1} here are constructed to represent bulk silica, they overestimate the density by 20%. This density difference could be enough to change the potential energy landscape, creating TLSs in the 0.1 to 0.3 eV range responsible for the excess loss compared to bulk experiments. A similar effect may be happening in IBS thin-film silica, where the deposition techniques lead to different constraints on the system, which causes the emergence of TLSs in the same range.

The choice to treat the attempt frequency (τ_0^{-1}) as an average prevents these calculations from capturing a complicated relationship between Q^{-1} and the frequency of the acoustic wave (ω). Within this approximation, increasing ω only affects Q^{-1} by broadening the low-temperature peak, increasing the peak magnitude, and shifting the peak to higher temperature. This effect matches the frequency dependence seen in bulk measurements, which suggests that Q_{bulk}^{-1} is created by a single transition with a consistent relaxation time across the ensemble of TLSs. However, the IBS measurements show more complicated behavior, which suggests that peaks do not consist of transitions with a single relaxation time. The two distinct transitions that create the low-temperature peak in Q_{corr}^{-1} reinforce that view. To capture the complicated dependence on ω , the model shown here must be expanded to calculate the relaxation time of each transition, which requires development of the computational methods used to generate input parameters for Q^{-1} . However, the advances in predictability shown in this paper demonstrate that the TLS model is sensitive enough to reproduce the fine details seen in experiment. We are currently exploring these ideas using the model presented in this paper, but they are beyond the scope of this work.

IV. CONCLUSION

In this paper, we demonstrate that calculating mechanical loss using a fully correlated TLS distribution yields qualitatively different features than a separated distribution, and reproduces the nonmonotonicity observed in ion-beam sputtered silica. All previous works use a separated distribution, which does not reproduce experimental results of either bulk or thin-film amorphous silica. While experimental measurements around 1000 Hz show a peak between 18 and 40 K depending on the sample preparation, the separated distribution shows a peak at 86 K and overestimate the internal friction Q^{-1} over 40 K by a factor of four to five. We show that the disagreement at low temperature arises because using a separable distribution for the number density of TLSs shifts the density to higher asymmetry, which prevents activation at low temperature. At higher temperature, which correlates to higher barrier

height, the separated distribution has highest density at low asymmetry. However, this is the exact opposite of what the correlated distribution shows, which is that as the barrier height increases, a larger range of asymmetry is possible. Because of this, the separable distribution activates more TLSs at higher temperature than are truly there.

Previous authors have introduced a cutoff in the separated distribution to artificially create a low-temperature peak, but our work shows that by using the fully correlated number density, this *ad hoc* choice is not necessary. We also show that the correlated distribution leads to a superior description of high-temperature behavior compared to a separated distribution with cutoff, where calculations using a correlated distribution find a second peak at 120 K. This nonmonotonic behavior is not observed in calculations using a separated distribution with cutoff and matches experimental measurements on ion-beam sputtered thin-film silica. These results suggest that to capture the complex behavior in Q^{-1} beyond the low-temperature peak, the fully correlated distribution must be used. This leads to agreement with IBS thin films up to at least ~ 150 K and may extend to room temperature with improved statistics.

By plotting $Q^{-1}(V, \Delta; T)$ [Eq. (13)], features in the internal friction can be connected to specific regions of the TLS distribution. Using this connection, characteristic transitions can be identified for each feature of Q^{-1} . Histograms of transition descriptors show that the mechanical loss calculated here contains three different features:

- (1) A sharp peak at 12 K, created by transitions with ~ 25 atoms which usually include a coordination change.
- (2) A broad low-temperature peak centered at ~ 30 K, created by transitions of ~ 50 atoms involving one to five oxygen rotations and coordination changes.
- (3) A peak at 114 K, created by transitions of ~ 75 atoms with 5+ coordination changes and oxygen rotations.

The results shown here suggest that the TLS model can capture excitations beyond the low-temperature peak, matching some of the complicated behavior seen in ion-beam sputtered silica. Calculating higher-temperature excitations relies on using the correct TLS distribution, which includes the correlation of V and Δ . Future studies into the dependence of Q^{-1} on density could explain the difference between IBS and bulk measurements, and could suggest avenues to lowering internal friction in amorphous oxides. The complicated relationship between Q^{-1} and frequency seen in thin-film silica shows the need to expand computational studies to calculate the attempt frequency for each TLS. However, the substantial agreement with experimentally measured mechanical loss shows that computational calculations can be a powerful tool in understanding the internal friction in amorphous oxides.

ACKNOWLEDGMENTS

The authors gratefully acknowledge support from Grant No. NSF/PHY-1068138. We also thank NERSC for computing resources.

[1] B. Abbott, R. Abbott, T. Abbott, M. Abernathy, F. Acernese, K. Ackley, C. Adams, T. Adams, P. Addesso, R. Adhikari *et al.*, *Phys. Rev. Lett.* **116**, 061102 (2016).

[2] G. M. Harry, A. M. Gretarsson, P. R. Saulson, S. E. Kittelberger, S. D. Penn, W. J. Startin, S. Rowan, M. M. Fejer, D. Crooks, G. Cagnoli *et al.*, *Classic. Quantum Gravity* **19**, 897 (2002).

- [3] G. M. Harry, H. Armandula, E. Black, D. Crooks, G. Cagnoli, J. Hough, P. Murray, S. Reid, S. Rowan, P. Sneddon *et al.*, *Appl. Opt.* **45**, 1569 (2006).
- [4] P. R. Saulson, *Phys. Rev. D* **42**, 2437 (1990).
- [5] H. B. Callen and R. F. Greene, *Phys. Rev.* **86**, 702 (1952).
- [6] W. Phillips, *J. Low Temp. Phys.* **7**, 351 (1972).
- [7] P. W. Anderson, B. Halperin, and C. M. Varma, *Philos. Mag.* **25**, 1 (1972).
- [8] J. Jäckle, *Z. Phys.* **257**, 212 (1972).
- [9] W. Phillips, *Rep. Prog. Phys.* **50**, 1657 (1987).
- [10] K. Gilroy and W. Phillips, *Philos. Mag. B* **43**, 735 (1981).
- [11] X. Liu, D. R. Queen, T. H. Metcalf, J. E. Karel, and F. Hellman, *Phys. Rev. Lett.* **113**, 025503 (2014).
- [12] D. R. Queen, X. Liu, J. Karel, T. H. Metcalf, and F. Hellman, *Phys. Rev. Lett.* **110**, 135901 (2013).
- [13] X. Liu, B. E. White Jr, R. O. Pohl, E. Iwaniczko, K. M. Jones, A. H. Mahan, B. N. Nelson, R. S. Crandall, and S. Veprek, *Phys. Rev. Lett.* **78**, 4418 (1997).
- [14] D. Tielbürger, R. Merz, R. Ehrenfels, and S. Hunklinger, *Phys. Rev. B* **45**, 2750 (1992).
- [15] O. Anderson and H. Bömmel, *J. Am. Ceram. Soc.* **38**, 125 (1955).
- [16] M. E. Fine, H. Van Duyn, and N. T. Kenney, *J. Appl. Phys.* **25**, 402 (1954).
- [17] U. Bartell and S. Hunklinger, *J. Phys. Colloq.* **43**, C9-489 (1982).
- [18] D. G. Cahill and J. Van Cleve, *Rev. Sci. Instrum.* **60**, 2706 (1989).
- [19] A. K. Raychaudhuri and S. Hunklinger, *Z. Phys. B Condens. Matter* **57**, 113 (1984).
- [20] B. E. White Jr. and R. O. Pohl, *Phys. Rev. Lett.* **75**, 4437 (1995).
- [21] I. Martin, R. Nawrodt, K. Craig, C. Schwarz, R. Bassiri, G. Harry, J. Hough, S. Penn, S. Reid, R. Robie *et al.*, *Classic. Quantum Gravity* **31**, 035019 (2014).
- [22] R. Hamdan, J. P. Trinastic, and H. Cheng, *J. Chem. Phys.* **141**, 054501 (2014).
- [23] J. P. Trinastic, R. Hamdan, C. Billman, and H.-P. Cheng, *Phys. Rev. B* **93**, 014105 (2016).
- [24] K. Topp and D. G. Cahill, *Z. Phys. B Condens. Matter* **101**, 235 (1996).
- [25] J. Reinisch and A. Heuer, *Phys. Rev. Lett.* **95**, 155502 (2005).
- [26] R. Vacher, E. Courtens, and M. Foret, *Phys. Rev. B* **72**, 214205 (2005).
- [27] F. Travasso, L. Bosi, A. Dari, L. Gammaitoni, H. Vocca, and F. Marchesoni, *Mater. Sci. Eng.: A* **521-522**, 268 (2009).
- [28] B. Halperin, *Ann. NY Acad. Sci.* **279**, 173 (1976).
- [29] J. Black, *Phys. Rev. B* **17**, 2740 (1978).
- [30] A. J. Leggett and D. C. Vural, *J. Phys. Chem. B* **117**, 12966 (2013).
- [31] W. Köhler and J. Friedrich, *Phys. Rev. Lett.* **59**, 2199 (1987).
- [32] R. Jankowiak, G. Small, and B. Ries, *Chem. Phys.* **118**, 223 (1987).
- [33] W. Kauzmann, *Rev. Mod. Phys.* **14**, 12 (1942).
- [34] J. Horbach and W. Kob, *Phys. Rev. B* **60**, 3169 (1999).
- [35] Computer code DLPOLY, version 1, W. Smith, T. Forester, I. Todorov, and U. Cheshire (Science and Technology Facilities Council, Daresbury Laboratory, UK, 2012).
- [36] B. W. H. van Beest, G. J. Kramer, and R. A. van Santen, *Phys. Rev. Lett.* **64**, 1955 (1990).
- [37] J. Yu, R. Devanathan, and W. J. Weber, *J. Mater. Chem.* **19**, 3923 (2009).
- [38] Z. Raza, I. A. Abrikosov *et al.*, *J. Phys.: Condens. Matter* **27**, 293201 (2015).
- [39] B. Lunin, *Physical and Chemical Bases for Development of Hemispherical Resonators for Solid-state Gyroscopes* (Moscow Aviation Institute, Moscow, 2005).
- [40] G. M. Bartenev, V. A. Lomovskoi, and G. M. Sinitsyna, *Inorg. Mater.* **32**, 671 (1996).
- [41] B. Mantsi, M. Bauchy, and M. Micoulaut, *Phys. Rev. B* **92**, 134201 (2015).